DEM EXTRACTION OF THE BASAL TOPOGRAPHY OF THE CANADIAN ARCHIPELAGO ICE CAPS VIA 2D AUTOMATED LAYER-TRACKER

Mohanad Al-Ibadi[1], Jordan Sprick[1], Sravya Athinarapu[1], Theresa Stumpf[1], John Paden[1], Carl Leuschen[1], Fernando Rodríguez[1], Mingze Xu[2], David Crandall[2], Geoffrey Fox[2], David Burgess[3], Martin Sharp[4], Luke Copland[5], and Wesley Van Wychen[5]

[1]Center for Remote Sensing of Ice Sheets, University of Kansas, USA, [2]School of Computing and Informatics, Indiana University, USA, [3]Geological Survey of Canada, [4]Dept. of Earth and Atmospheric Sciences, University of Alberta, Canada, [5]Dept. of Geography, Environment and Geomatics, University of Ottawa, Canada

ABSTRACT

The basal topography of most of the glaciers that drain the ice caps of the Canadian Arctic Archipelago is largely unknown. To measure the basal topography, NASA Operation IceBridge flew a radar depth sounder in a wide swath mode with three transmit beams to image the glacier beds during three flights over the archipelago in 2014. We describe the measurement setup of the radar system, the algorithms used to process the data to produce a 3D image of the glacier bed, show digital elevation model (DEM) results of the beds, and provide a basic assessment of the tracking algorithm used to extract the DEM.

Index Terms— synthetic aperture radar imaging, ice

1. INTRODUCTION

The basal topography of outlet glaciers draining the Canadian Arctic Archipelago (CAA) ice caps is largely unknown. This basal topography is needed for calculating these ice caps' present sea level contribution using the surface mass balance and discharge method, and to project their future sea level contributions using ice flow model studies [1]. During the NASA Operation IceBridge 2014 arctic campaign, the Multichannel Coherent Radar Depth Sounder (MCoRDS) used three transmit beams (left, nadir, and right) time multiplexed to illuminate a wide swath in a single pass during three flights over the archipelago. Fig. 1 illustrates the system geometry for the data collection.

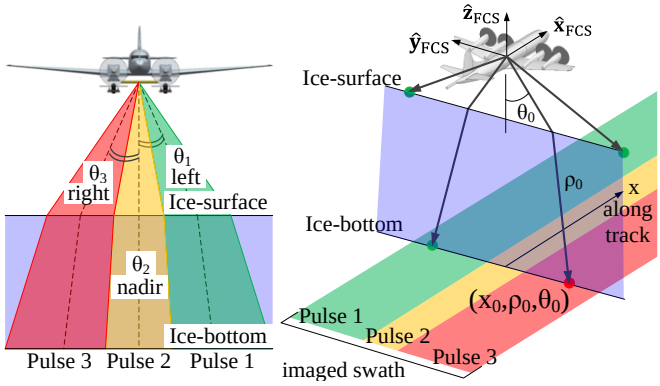

Fig. 1. System geometry.

To generate a digital elevation model, we use pulse compression, synthetic aperture radar (SAR) processing, and array processing to form a 3D image of the ice base. From these images we can track the ice-bottom, estimate the ice thickness, and obtain other useful information. *The focus of this work is on generating an ice-bottom digital elevation model from multibeam radar depth sounder data.*

The array processing in this work follows the method described in [2] which produces a 3D matrix of voxels. We have added an additional step to calibrate the array by equalizing the signals at each element for a nadir target and by adjusting the steering vector angles based on a least squares fit to known digital elevation model ice-surface data. These processing steps are described in section 3.1.

Because of the high volume of data produced by 3D imaging, manual tracking of the ice-bottom is impractical on a large scale. To solve this problem, *we used an automated technique for extracting ice-bottom surfaces by viewing the task as an inference problem on a probabilistic graphical model.* We first estimate layer boundaries to generate a seed surface, and then incorporate additional sources of evidence, such as ice masks, surface digital elevation models, and feedback from human users, to refine the surface in a discrete energy minimization formulation. This ice-surface and ice-bottom tracking algorithm is described in sections 3.2.

The width of the resultant tracked ice-bottom image at the nominal flight altitude of 3000 ft above ground level (AGL) is approximately 3 km in most cases. Since the glacier channels in the archipelago are often narrower than this, the radar imaging, in these instances, was able to measure the full glacier cavity in a single pass. To validate the automated tracking, we compare manually tracked "ground truth" to the automated tracking algorithms. These results are discussed in Section 4.

2. HARDWARE DESCRIPTION

MCoRDS [3] consists of three main subsystems: digital, RF, and antennas. Table 1 shows the radar system parameters. To increase the imaged swath, the radar was set to a multibeam

transmission mode with three transmit beams steered to the left (-30^o), nadir (0^o), and right (30^o). The beam parameters are given in Table 2. The transmit beamwidth with the tapered Hanning window produces a beam with most of the power in a 30° wide beamwidth.

Table 1: Radar System Parameters

Parameter	Value
Radar carrier-frequency	195 MHz
Signal bandwidth	30 MHz
Transmit pulse duration	3 μs
TX antennas	7 Dipoles
RX antennas	15 Dipoles
PRF	12 KHz
Effective Storage PRF 3 Beams Multiplexed, 13 stacked pulses	307 Hz

Table 2: Transmit Beam Parameters

Waveform	Look Angle	Attenuation	Weights
1	-30° (left)	15 dB	Hanning
2	0° (nadir)	20 dB	Hanning
3	+30° (right)	15 dB	Hanning

The digital section consists of a waveform generator for each transmit antenna and an analog-to-digital-converter (ADC) for each receive antenna. The waveform generators are individually amplitude, phase, and time-shifted to produce a Tukey-weighted linear-FM chirp, beam steered in the desired direction. The system cycles every 13 pulses between left, nadir, and right beams. Each batch of 13 pulses captured by an ADC, is averaged in hardware, and then stored to disk creating 15 independent streams of data, one per antenna.

The RF transmit section consists of power amplifiers, bandpass filters, and switches needed to pre-condition the generated pulses before injecting them into the air through the transmit antenna elements.

There are fifteen receive antenna elements divided into 3 subarrays. In this work, we only make use of the 7 receive elements in the center subarray, which has a length of 4.5 m, to avoid grating lobe issues incurred when coherently combining the 3 subarrays which are separated by substantial baselines.

The duration of the transmitted pulse, 3 μs, was chosen as the longest pulse duration that would guarantee capture of the ice-surface. We assumed a minimum altitude of 2250 ft AGL and about 1.5 μs for the center 7 elements to switch from transmitting to receiving. Due to the thin ice (<1000m), we operated with a single receiver gain setting for the entire range line and chose the gain to be the highest setting that still guaranteed that the surface return would not saturate the receiver.

For a platform speed of $v = 124\frac{m}{s}$, the Nyquist criterion requires $PRF = \frac{4v}{\lambda_c} = 322$ Hz. The actual recording rate of 307 Hz leads to some ambiguity in near grazing angle sidelobes in along-track. However, these look angles are not used because basal ice scattering is undetectable at these angles.

3. ALGORITHM DESCRIPTION

3.1. Radar Processing and 3D Image Formation

Here, we give a general description of the basic radar processing steps that lead to the formation of the tomographic 3D image. A target can be located by its range ρ, along-track position x, and its direction of arrival (elevation) angle θ. This coordinate system for an example target, indicated by a red dot, is illustrated in Fig. 1. It is a cylindrical coordinate system modified for refraction at the ice-surface. The target location (x, ρ, θ) is estimated via three main processing steps: 1) pulse compression of the linear-FM pulse to resolve the range of the target, 2) SAR processing to resolve the along-track position, and 3) array processing to estimate the elevation angle. The ice-surface must also be known to account for refraction.

To maintain radiometric accuracy, the raw data are converted from quantization to receiver input voltage which accounts for variable-gain effects of the receiver. Filters are normalized to produce properly scaled estimates of signal strength. Finally, transmit array and receive array calibration are performed on each of the channels to remove amplitude, time, and phase errors between the antenna array elements.

Pulse compression is then applied to resolve the pre-conditioned data in the range dimension by frequency domain matched filtering with a Hanning windowing to suppress range sidelobes. SAR processing is then applied to focus the data in the along-track dimension. The main part of this step is a modified frequency-wavenumber migration algorithm described in [4] that is designed for layered media. Rapid fluctuations in the trajectory relative to the nominal SAR aperture length are compensated for by time shifting signals along the aperture to mimic a smooth flight trajectory with a squint angle of nadir. After SAR processing, these time delays are removed to preserve the actual phase centers of the measurements. Fluctuations in platform velocity are handled by uniformly re-sampling the radar data in along-track using a sinc-interpolation kernel.

After range and azimuth processing, 2D echogram images of the scene can be formulated as along-track position versus travel time or range assuming the speed of propagation is known. To obtain a 3D tomographic image of the ice-bottom, the elevation angles of the targets need to be estimated. This problem can be formulated as a direction of arrival (DoA) problem [2]. In this work, we use the narrowband MUltiple Signal Classification (MUSIC) technique to estimate the directions of the signals impinging on the sensor-array elements of the airborne radar.

For MUSIC, we first must estimate the number of separable targets, Q, which reside in the SAR pixel. Ignoring englacial targets, there are typically four separable signals in a single range bin: left/right ice-surface and left/right ice-bottom as

shown by the green and red circles in Fig. 1. However, with transmit beamforming, usually only two signals dominate, so we set $Q = 2$. For example, in the left transmit beam, the left ice-surface and left ice-bottom targets tend to dominate. For each of the 7 sensors, a SAR image is formed. We use MUSIC as a beam-former to combine these 7 images and scan θ to produce a 3D image. To improve the accuracy of the MUSIC steering vectors, the ice-surface DEM was used to calibrate the steering vectors using a low order polynomial least squares fit of the error between the radar derived ice-surface and an existing ice-surface DEM [5].

After forming a 3D image from each transmit beam, the three images are merged using a weighted sum to produce a single digitally-formed wide swath beam as shown in Fig. 2. Weights are normalized Gaussian functions proportioned according to the transmit direction.

3.2. 2D Layer-Tracking Algorithm

As mentioned, manual tracking of the ice-bottom is impractical on a large scale. To solve this problem, we have implemented an automated technique for extracting ice-bottom surfaces. We first generate a seed surface subject to a set of constraints which account for both the mismatch between the radar data and the model parameters as well as the smoothness of the estimated surface. Additional sources of evidence are then incorporated to refine the surface in a discrete energy minimization formulation, using the Sequential Tree Reweighted Message Passing (TRW) algorithm [6,7].

The additional sources of evidence include human-labeled ground truth, the ice-surface digital elevation model (DEM), and the ice mask of the land surface.

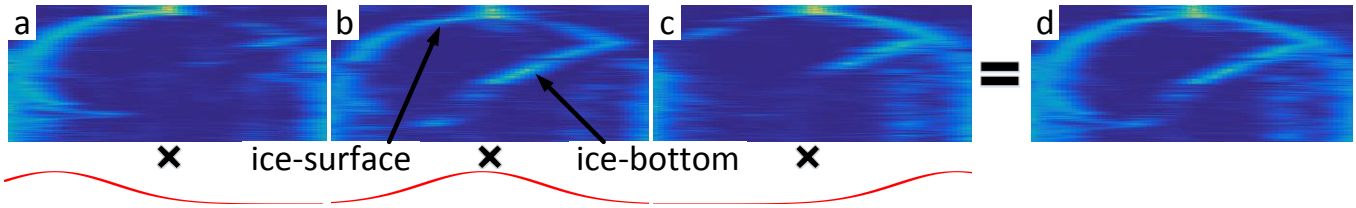

Fig. 2. Left (a), nadir (b), and right (c) beams and their corresponding weight functions in red. d. Combined image.

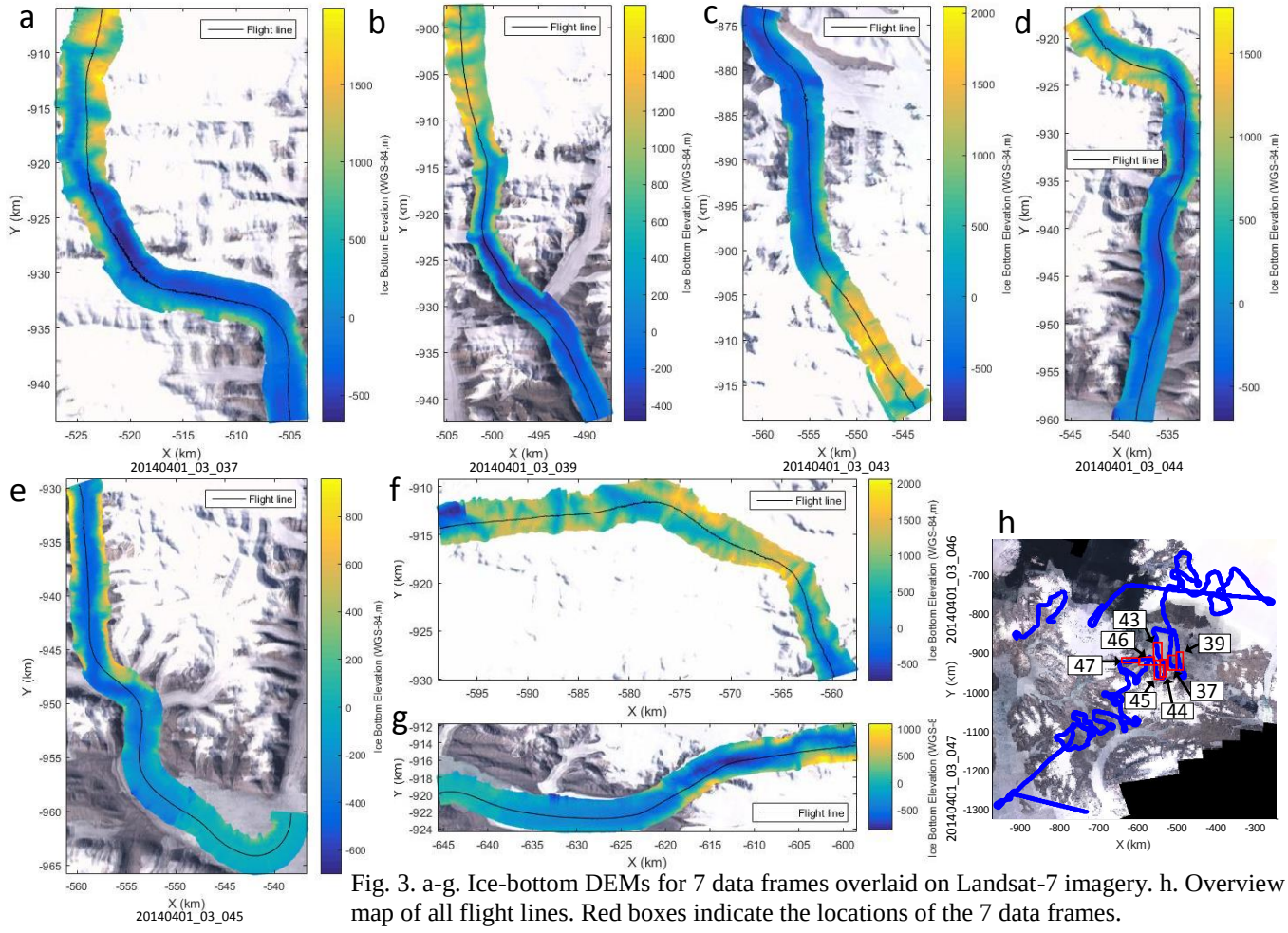

Fig. 3. a-g. Ice-bottom DEMs for 7 data frames overlaid on Landsat-7 imagery. h. Overview map of all flight lines. Red boxes indicate the locations of the 7 data frames.

The human-labeled ground truth points indicate where the ice-bottom layer should pass through. However, they are not always accurate at the pixel-level since it is difficult for an operator to be both precise and efficient. To decouple from the ground truth errors, we consider two labels as the same when their difference is within a few pixels and then rely on the image characteristics to drive the inference model to a more precise answer.

For each angle of incidence in the 3D image, the surface DEM is used to find an estimate of the range to the surface. The automatic tracker tunes the tracker parameters to match this reference and create stochastic parameters associated with the nearby arrangement of image intensities. These parameters are then used to track the unknown ice-bottom.

The ice mask is a binary raster that is used to determine at each angle of arrival whether there is ice or not. When estimating the location of the ice-bottom, the automatic tracker applies a higher cost to very thin ice because the ice-bottom estimate tends to track ice-surface sidelobes without this. However, where there is no ice, the ice-surface and ice-bottom need to merge and this additional cost prevents that. With an ice mask available, the automatic surface tracker alters the cost calculation accordingly and forces the ice-surface and ice-bottom to merge where there is no ice.

4. RESULTS AND DISCUSSION

Fig. 3a-g show the resultant basal topography for seven data frames from the CAA where we applied our 2D automated layer-tracker. Fig. 3h shows the locations of each frame. All are overlaid on Landsat-7 imagery.

Three statistical properties were used to assess the automated tracking algorithm: the mean of the absolute error, median of the absolute error, and precision of the correct human-labeled ground truth pixels over the whole surface. The error is measured as the range bin difference between completely automated results and results that were hand corrected.

Table 2 shows a comparison of our results versus published results. Our method has substantially lower mean error and median error compared with the Viterbi method and methods described in [8] and [9]. More details on the mathematical foundation of the layer tracker with detailed interpretation of these results is given in [10].

Table 2. Comparison of Automated Tracking Algorithms.

	Mean Error	Median Error	Precision
[8]	122.56	59.0	0.34%
[9]	28.9	10	4.9%
Viterbi [10]	13.3	3.0	20.2%
TRW [10]	11.9	2.0	36%

5. CONCLUSION

We collected swath mode radar data with settings specifically set for the imaged radar scene. These data were processed using 3D imaging routines that included new calibration techniques not previously reported. Also, a new surface tracking algorithm was developed. Ice-surface and ice-bottom DEMs were generated from these tracked surfaces. Finally, the performance of the algorithm versus human tracking was compared against previous image tracking algorithms with positive results.

6. ACKNOWLEDGEMENTS

We acknowledge support from NASA (NNX16AH54G), NSF (1443054, 0424589), Canadian Space Agency, and NSERC. Also, we gratefully acknowledge Prof. P. Gogineni for his vision and the technical contributions that resulted in this work.

7. REFERENCES

[1] A.Gilbert, G.Flowers, G.Miller, B.Rabus, W.Van Wychen, A.Gardner, L.Copland, "Sensitivity of Barnes Ice Cap, Baffin Island, Canada, to Climate State and Internal Dynamics ," Journal of Geophysical Research – Earth Surface, vol.121, Issue 8, 2016.

[2] J. Paden, T. Akins, D. Dunson, C. Allen, P. Gogineni, "Ice-Sheet Bed 3-D Tomography," Journal of Glaciology, vol.56, no.195, pp. 3-11, 2010.

[3] F. Rodríguez-Morales, P. Gogineni, C. Leuschen, J. Paden, J. Li, C. Lewis, B. Panzer, D. Gomez-García Alvestegui, A. Patel, K. Byers, R. Crowe, K. Player, R. Hale, E. Arnold, L. Smith, C. Gifford, D. Braaten, C. Panton, "Advanced Multifrequency Radar Instrumentation for Polar Research," IEEE Trans. Geosci. Remote Sens., vol.52, no.5, pp. 2824-2842, 2014.

[4] C. Leuschen, S. Gogineni, D. Tammana, "SAR processing of radio echo sounder data," International Geoscience and Remote Sensing Symposium (IGARSS), pp. 2570-2572, 2000.

[5] J. Korona, E. Berthier, M. Bernard, F. Remy, E. Thouvenot, "SPIRIT. SPOT 5 stereoscopic survey of Polar Ice: Reference Images and Topographies during the fourth International Polar Year (2007-2009)," ISPRS Journal of Photogrammetry and Remote Sensing, vol.64, Issue 2, pp. 204-212, 2009.

[6] D. Koller, N. Friedman, "Probabilistic graphical models: principles and techniques," The MIT Press, Cambridge, Massachusetts, London, England, 2009.

[7] V. Kolmogorov, "Convergent tree-reweighted message passing for energy minimization," IEEE Trans. Pattern Anal. Mach. Intell, vol. 28, no. 10, pp. 1568–1583, 2006.

[8] D. Crandall, G. Fox, J. Paden, "Layer-finding in radar echograms using probabilistic graphical models," 21st IEEE International Conference on Pattern Recognition (ICPR), pp. 1530-1533, 2012.

[9] S. Lee, J. Mitchell, D. Crandall, G. Fox, "Estimating bedrock and surface layer boundaries and confidence intervals in ice sheet radar imagery using MCMC," IEEE International Conference on Image Processing (ICIP), pp. 111–115, 2014.

[10] M. Xu, D. Crandall, G. Fox, J. Paden," Automated Extraction of Ice Bottom Surfaces Using Probabilistic Graphical Models," in preparation.